MULTIFUNCTION IMPULSE RADIATING ANTENNAS: THEORY AND EXPERIMENT

Everett G. Farr[1], Carl E. Baum[2], William D. Prather[2] and Leland H. Bowen[1]
[1]Farr Research, Inc.
Albuquerque, NM 87123
[2]Air Force Research Laboratory
Kirtland AFB, NM 87117

I. ABSTRACT

A Multifunction IRA is an extension of a standard Impulse Radiating Antenna that has the additional flexibility of an adjustable beamwidth. This adjustability is implemented by defocusing the feed, in order to select between a narrow or broad beam. We provide here the theory of operation of the antenna, for both in-focus and out-of-focus situations. Furthermore, we built and tested a design with a 46 cm diameter. We found good agreement of the experiment with theory.

II. INTRODUCTION

A reflector Impulse Radiating Antenna (IRA) consists of a parabolic reflector with a TEM feed. This class of antenna has a considerable body of literature associated with both its analysis and measurements [1-3]. One issue that has been raised concerning this type of antenna, however, is that the beamwidth is too narrow for many applications. In order to broaden the beam, we introduce the Multifunction IRA, or MIRA.

The principle behind the MIRA is quite simple. The feed point of an IRA is normally at the geometric focus of a parabolic reflector. In a MIRA, we defocus the feed arms slightly, by placing the feed point somewhat closer to the dish than its normal position at the focus of the reflector.

If one can add a mechanical control to the feed point location, then one can have a single antenna with a narrow or broad beam, as required. This results in a single antenna with very broad bandwidth and beamwidth control. Such an antenna may be useful in applications where a single antenna must serve multiple functions due to limited aperture space. In this note we develop the theory of such a device, and we describe the fabrication and testing of a prototype design.

The theory developed here is based on the quasistatic electric field in an aperture. In previous papers [2-8], we have developed a number of techniques for calculating the radiated field when an aperture field is turned on uniformly, all at the same time. With a defocused aperture, however, the aperture is turned on gradually, beginning at the center. The theory is modified here that takes this gradual turnon into account. We provide here theoretical calculations of the radiated impulse in the H- and E-planes, for both focused and defocused aperture positions.

In addition, an experimental prototype was developed with a 46 cm (18 in) diameter reflector using four feed arms with an adjustable position. The position is controlled by a servo mechanism that is controlled by a personal computer.

By including computer control in the design, we allow a great deal of flexibility in system design. For example, one might use the MIRA as part of a radar system that can operate in either search mode, which requires a broad beamwidth, or tracking mode, which requires a narrow beamwidth. A block diagram of such an arrangement is shown in Figure 2.1. The controller would select which of two radar systems would be fed into the antenna. The controller would also set the antenna feed position, in order to control the beamwidth.

The field is measured using TEM sensors. These were developed based on an idea by C. J. Buchenauer[9] to enhance signal-to-noise ratio with very fast, low-voltage pulsers. These sensors are replicating sensors, not the derivative sensors that are perhaps more commonly used. We calibrate these sensors using two identical sensors.

Note that this work was first reported in [14]. It is refined here by using improved sensors and by building an improved feed point.

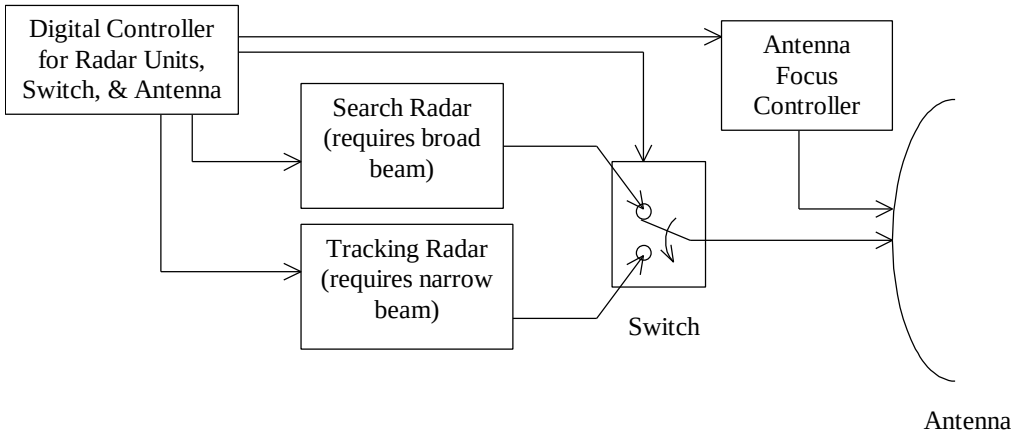

Figure 2.1. Control of the RF switch and antenna focus using a digital controller.

III. Modification of Theory to Include Defocused Aperture

To calculate the radiated field for the defocused aperture, it is first necessary to review the theory for the focused aperture radiation [2,3]. The theory for the defocused aperture is a straightforward perturbation on the theory for the focused aperture. To do so, we need to return to more general expressions for the field radiated from an aperture. Thus, we have the field radiated from an aperture, from [10, eqn 2.7]

$$\begin{aligned} \vec{E}(\vec{r}, s) &= \frac{1}{2\,p\,r} \iint_{S_a} g\left[\vec{1}_z \times \vec{E}_t(x', y', s) \times \vec{1}_R\right] e^{-gR}\, dA \\ &= \frac{s}{2\,p\,r\,c} \iint_{S_a} \left[\vec{1}_z \times \vec{E}_t(x', y', s) \times \vec{1}_R\right] e^{-sR/c}\, dA \end{aligned} \tag{3.1}$$

where primed coordinates refer to the aperture plane, and unprimed coordinates refer to the observation point. Furthermore, $\vec{E}_t(x', y', s)$ is the tangential aperture field in the aperture plane, and S_a is the aperture surface. The aperture plane is the x'-y' plane (at z'=0). Note that the above equation differs from [10 eqn 2.7] by retaining only the far-field (1/r) term, and by substituting $g = s/c$. The expressions for r and R are

$$r = \sqrt{x^2 + y^2 + z^2}$$
$$R = \sqrt{(x - x')^2 + (y - y')^2 + (z - z')^2} \tag{3.2}$$

We will shortly specialize the above expressions for the radiated field to the H- and E-planes, but before we do so, we first wish to describe the form of the aperture field.

The form of the tangential aperture electric field is

$$E_y(t) = -\frac{V_o}{\Delta u}\,\frac{\partial u(x', y')}{\partial y'}\,W(t) \qquad u(\zeta) = \mathrm{Re}(w_4)$$
$$w_4(\zeta) = w_2(\sqrt{2\zeta}\ /\ a + 1) + w_2(\sqrt{2\zeta}\ /\ a - 1) \qquad w_2 = \ln\left(\frac{\zeta - ja}{\zeta + ja}\right) \tag{3.3}$$

where $u(x', y')$ is the potential function described previously in [2, eqns. (2.2)-(2.3)]. (Note that there was an error in the original expression for $w_4(\zeta)$ appearing in [14 eqn 4.2], which is corrected here.) Furthermore, $W(t)$ is a window function that takes into account the gradual illumination of the aperture. This is illustrated in Figure 3.1. Thus, $W(t)$ is a window that is circular in shape, with a radius described by $Y_a(t')$. We assume that the curved phase front first touches the center of the aperture at $t' = 0$, so at $Y_a(t'=0) = 0$. Furthermore, the instant where the aperture is first completely filled is denoted by t'_{max}, so $Y_a(t'_{max}) = Y_{a,max}$.

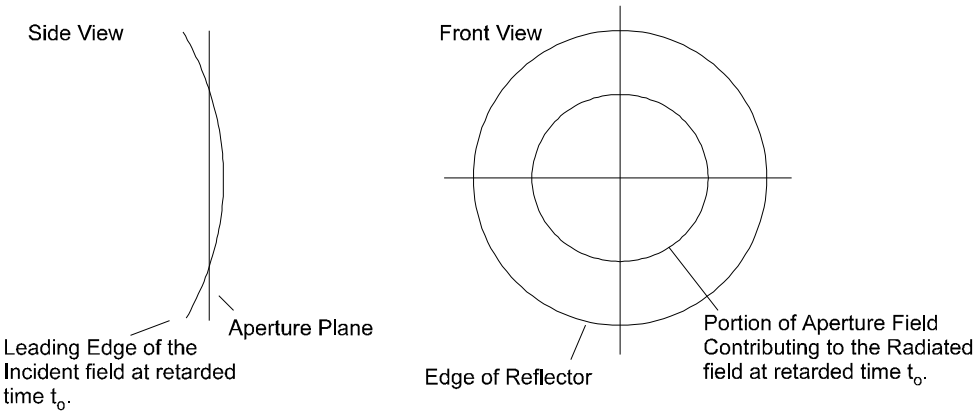

Figure 3.1. Illustration of how a defocused aperture is filled gradually by the incident field (left). The portion of the aperture plane contributing to the aperture field is shown on the right.

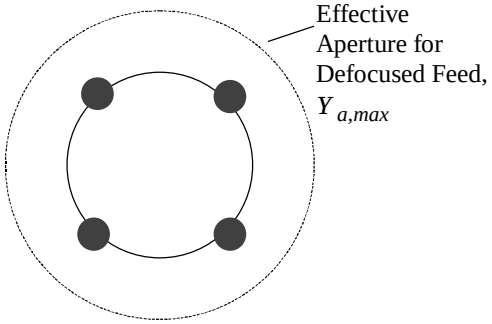

Figure 3.2. The effective aperture when a rigid feed arm assembly is pushed toward the reflector.

Note that some care must be taken when determining the position where the above potential function is evaluated. The position in the aperture plane, (x', y'), must be mapped onto a position in a flat virtual plane (x_v, y_v), using stereographic projections. If we describe a position on the aperture in the polar (cylindrical) coordinates, (Y', f'), it is necessary to map the position on the aperture onto a virtual plane, described by (Y_v, f_v), shown in Figure 3.2. To do so, we use

geometric optics to trace the ray that arrives at (f',Y'). This ray has an origin at the feed point, and it points in the direction (q_{inc}, f_{inc}). Due to symmetry, we have

$$\phi' = \phi_{inc} = \phi_v \tag{3.4}$$

so we have only left to find Y_v.

To find Y_v, we first find q_{inc} by geometric optics and ray tracing. In other words, we find the angle of departure of the ray that begins at the feed point and arrives at (Y', f'). Thus, having found q_{inc}, we need only find a relationship between q_{inc} and Y_v. The geometry is shown in Figure 3.3.

To complete the process of calculating Y_v, we compare the stereographic projection of (Y', f') to that of the charge center of the feed arms. We know the charge center of the feed arms projects onto the unit circle in the virtual plane, so $Y_{v,o} = 1$. Now by taking a ratio of stereographic projections,

$$= 2F \tan(\theta / 2) \tag{3.5}$$

we obtain

$$\begin{aligned} v &= {}_{v,o} \frac{\tan(\theta_{inc} / 2)}{\tan(\theta_{inc,o} / 2)} \\ \phi_v &= \phi' \end{aligned} \tag{3.6}$$

The only remaining unknown in this equation is the incident angle of the charge center. This is found from the *F*/*D* ratio of the reflector, f_d, so

$$\theta_{inc,o} = \arctan\left[\frac{1}{2 f_d - 1/(8 f_d)}\right] \tag{3.7}$$

and we now have both Y_v,and f_v. From these two, we can calculate (x_v,y_v), so we have completed our procedure for mapping (x',y') into (x_v,y_v).

Having described the aperture fields, we now restrict the expression for the radiated field, (3.1), to the H-plane and E-plane. We begin with the H-plane.

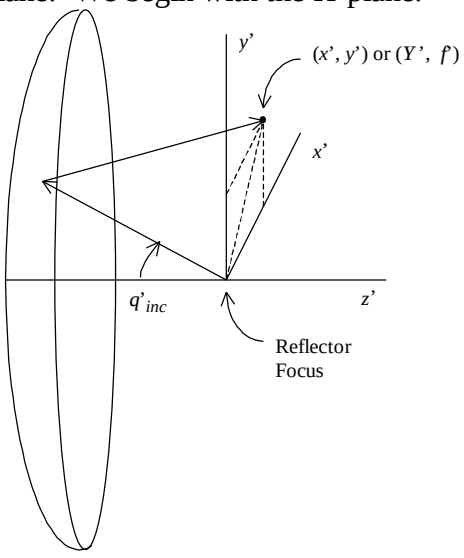

Figure 3.3. The ray trace from the focus to a point in the aperture plane.

A. H-Plane Calculation

In the H-plane the dominant component of the radiated field is the *y*-component. Furthermore, only the *y*-component of the aperture field contributes to the *y*-component of the radiated field due to symmetry. Thus, after restricting the tangential field to the *y*-component, we have

$$\begin{aligned} \vec{1}_z \times \tilde{\tilde{E}}_t(x', y', s) \times \vec{1}_R &= \vec{1}_y \ \tilde{E}_y(x', y', s) \ \cos(q) \\ R &\cong r - x' \sin(q) \end{aligned} \tag{3.8}$$

Substituting the above relationships into (3.1), we have, in both frequency and time domains,

$$\begin{aligned} \tilde{E}_y^{(h)}(q, s) &= \frac{s \cos(q)}{2 p r c} \iint_{S_a} \tilde{E}_y(x', y', s) \ e^{-(s/c)(r - x' \sin(q))} \ dA \\ E_y^{(h)}(q, t) &= \frac{\cos(q)}{2 p r c} \frac{d}{dt} \iint_{S_a} \tilde{E}_y(x', y', \ t - (r - x' \sin(q)) / c) \ dA \end{aligned} \tag{3.9}$$

where the superscript (h) indicates that the expression is specific to the H-plane. For simplicity, we convert to retarded time, $t' = t - r / c$, so

$$E_y^{(h)}(q, t') = \frac{\cos(q)}{2 p r c} \frac{d}{dt} \int dx' \int dy' \ E_y(x', y', t' + (x' / c) \sin(q)) \tag{3.10}$$

We now need to account for the time-varying nature of S_a. As stated previously, the aperture expands as a function of time, with a radius $Y_a(t')$. Thus, the limits of integration over the aperture change with time. Let us define

$$\begin{aligned} {}^{(h)}(x', t') &= -\frac{1}{V_o} \int_{-y_{max}(x't')}^{y_{max}(x', t')} dy' \ E_y(x', y') \\ y_{max}(x', t') &= \begin{cases} 0 & t' \ \ 0 \\ \sqrt{a^2(t') - x'^2} & 0 \ \ t' \ \ t_{max} \\ a, max & t' \ \ 0 \end{cases} \end{aligned} \tag{3.11}$$

This is closely analogous to [3, eqn. (4.5)], with the exception that there is an additional time dependence. The integration is carried out along a straight line of constant x', with limits that are determined by $W(t)$, the window function that describes the effective aperture radius as a function of t'. If we now combine the above expression with (3.3), we have

$${}^{(h)}(x', t') = \frac{2}{u} \ u(x', y_{max}(x', t')) \tag{3.12}$$

By combing equations (3.10-3.12) we have

$$E_{y, step}^{(h)}(q, t') = -\frac{V_o}{2 p r c} \cos(q) \frac{d}{dt} \int dx' \ \Phi^{(h)}(x', \ t' - (x' / c) \sin(q)) \tag{3.13}$$

This is now in a form that can be implemented numerically. Note that one can tabulate ${}^{(h)}(x', t')$ in order to avoid repetitive calculations. Then, $E_{y,step}^{(h)}(\theta, t')$ is calculated by a one-dimensional integral. Thus, we have successfully converted a double integral over the aperture to a single integral, which should be more numerically efficient. Note also that when calculating $u(x', y')$ it is necessary to calculate it into the virtual plane, as shown in equation (3.6). To find the response to a standard Gaussian pulse, we convolve the above step response with the derivative of the Gaussian, as shown previously in [2, eqns. 4.5-4.7].

B. E-Plane Calculation

Next, we calculate the radiated field in the E-plane. The derivation is very similar to that in the H-plane. The dominant component is the q- component , and once again, we need only calculate the y-component of the aperture field due to symmetry. This leads to

$$\begin{aligned} \vec{1}_z \times \tilde{\tilde{E}}_t(x', y', s) \times \vec{1}_R &= \vec{1}_y \ \tilde{E}_y(x', y', s) \\ R &\cong r - y' \sin(q) \end{aligned} \tag{3.14}$$

Substituting the above relationships into (3.1), we have, in both frequency and time domains,

$$\begin{aligned} \tilde{E}_q^{(e)}(q, s) &= \frac{s}{2 p r c} \iint_{S_a} \tilde{E}_y(x', y', s) \ e^{-(s/c)(r - x' \sin(q))} \ dA \\ E_q^{(e)}(q, t) &= \frac{1}{2 p r c} \frac{d}{dt} \iint_{S_a} \tilde{E}_y(x', y', \ t - (r - y' \sin(q)) / c) \ dA \end{aligned} \tag{3.15}$$

where the superscript (*e*) indicates that the expression is specific to the E-plane. As before, we convert to retarded time, $t' = t - r / c$, so

$$E_q^{(e)}(q, t') = \frac{1}{2 p r c} \frac{d}{dt} \int dy' \int dx' \ E_y(x', y', t' + (y' / c) \sin(q)) \tag{3.16}$$

We now need to account for the time-varying nature of S_a. As stated previously, the aperture expands as a function of time, with a radius $Y_a(t')$. Thus, the limits of integration over the aperture change with time. Let us define

$$\begin{aligned} {}^{(e)}(y', t') &= -\frac{1}{V_o} \int_{-x_{max}(y', t')}^{x_{max}(y', t')} dy' \ E_y(x', y') \\ x_{max}(y', t') &= \begin{cases} 0 & t' \ \ 0 \\ \sqrt{a^2(t') - y'^2} & 0 \ \ t' \ \ t_{max} \\ a,max & t' \ \ 0 \end{cases} \end{aligned} \tag{3.17}$$

This is closely analogous to [3, eqn. (4.7)], with the exception that there is an additional time dependence. The integration is carried out along a straight line of constant *y'*, with limits that are determined by *W*(*t*), the window function that describes the effective aperture radius as a function of *t'*. Note that one must take care in calculating ${}^{(e)}(x', t')$, due to the branch cut in the contour map. If we now combine the above with (3.3), we have

$$\begin{aligned} {}^{(e)}(y', t') &= \frac{1}{u} \int_{-x_{max}(t')}^{x_{max}(t')} \frac{\partial u}{\partial y} dx = -\frac{1}{u} \int_{-x_{max}(t')}^{x_{max}(t')} \frac{\partial v}{\partial x} dx \\ &= -\frac{2}{u} \left[v(x'_{max}(y', t'), y') - v(0, y') \right] \end{aligned} \tag{3.18}$$

where we have used the relationship $\partial u / \partial x = -\partial v / \partial y$. Care must be used in the application of the above formula for the difference of two *v*'s if a branch cut is crossed. In that case, a term of $2p$ must be subtracted from the difference in square brackets above. If we combine the above three equations, we have

$$E_{\theta, step}^{(e)}(\theta, t') = -\frac{V_o}{2 \pi r c} \frac{d}{dt} \int dy' \ \ {}^{(e)}(y', t' - (y' / c) \sin(\theta)) \tag{3.19}$$

This is now in a form that can be implemented numerically. Once again, we have converted a double integral over the aperture into a single integral, which is faster to calculate. Note that the position where the potential function $v(x', y')$ is calculated must be mapped onto the virtual plane as described in equation (3.6).

Having calculated the step response in both the H-and E-planes, we now convolve with a Gaussian, as shown previously in [2, eqns. 4.5-4.7], to obtain the far field As an example, we

calculated the radiated field in the H- and E-planes for a 46 cm (18 in) diameter reflector MIRA with $F/D = 0.5$, a risetime $t_d = 50$ ps and a feed impedance of 200 Ω.

Let us define now a ratio that describes the focal position. Let F be the focus of the reflector, and F_2 be the distance from the feed point to the reflector. Then we define a ratio

$$f_f = \frac{F_2}{F} \tag{3.20}$$

When the feed is located at the focus, $f_f = 1$. In our MIRA, we can adjust the focal point from $f_f = 0.7$ to $f_f = 1.0$. In the data we present here, $f_f = 0.7$, 0.85, and 1.0. The definition of f_f is shown in Figure 3.4.

The radiated field for $f_f = 1.0$ (feed at the focus) is shown in Figure 3.5. Both the H-plane and E-plane cuts are shown, for values off-boresight of 0, 7.5, and 15 degrees. We can clearly see that the field goes down as we proceed off-boresight in either plane. Furthermore, the radiated field for $f_f = 0.85$ and 0.7 are shown in Figures 3.6 and 3.7, respectively. From these plots, we can see that the peak field on boresight is reduced as we progressively defocus the antenna.

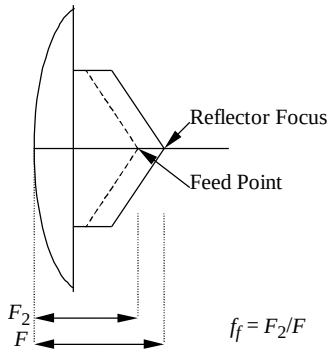

Figure 3.4. Definition of f_f.

Next, we need to define a beamwidth for this antenna, in order to compactly describe the data. We define the half field beamwidth (HFBW) as the angle between the two locations in a pattern cut where the field is down by half from the peak. Since we ran data at discreet angles off-boresight, the best we can do is estimate beamwidths. Furthermore, note that these beamwidths are specific to the particular choice of risetime, i.e., $t_d = 50$ ps. Finally, note that we estimate full beamwidths, not half beamwidths from boresight.

The HFBWs are provided in Table 3.1. From the data it is clear that the MIRA's beam broadens from about 8^o when in focus, to about 36^o when at the maximum defocus of $f_f = 0.7$. This is true in both the H- and E-planes. This is precisely the behavior we were hoping to find in this antenna.

Having demonstrated the relevant properties in theory, we now turn to experiment to verify the result.

Table 3.1. MIRA Half Field Beam Widths

	Half Field Beam Width (HFBW)	
$f_f = F_2/F$	H-Plane	E-Plane
1.00	8^o	10^o
0.85	15^o	15^o
0.70	36^o	36^o

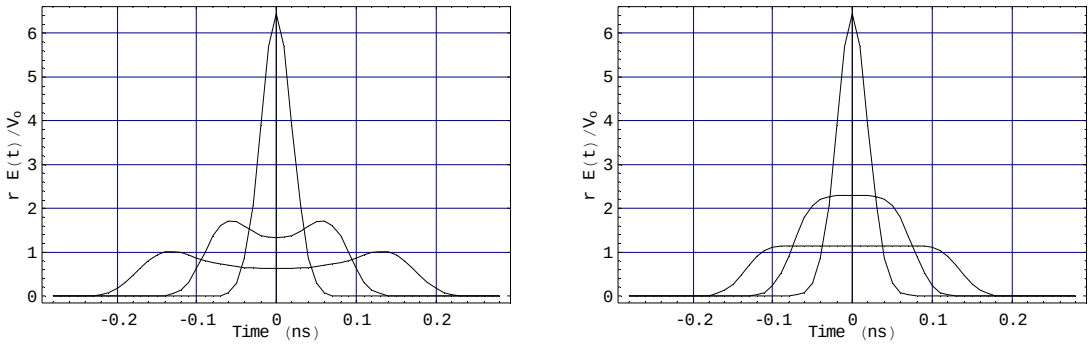

Figure 3.5. MIRA radiated field, f_f = 1.0 (in focus), H-plane (left) and E-plane (right), at angles of 0, 7.5, and 15 degrees off-boresight.

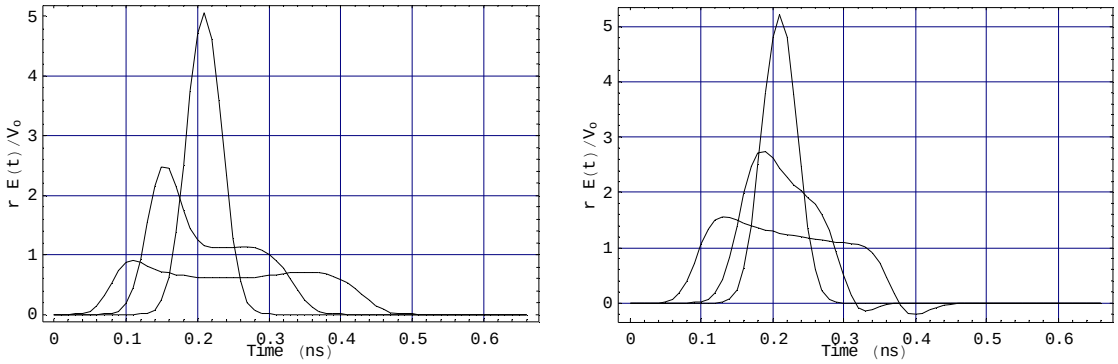

Figure 3.6. MIRA radiated field, f_f = 0.85, H-plane (left) and E-plane (right), at angles of 0, 7.5, and 15 degrees off-boresight.

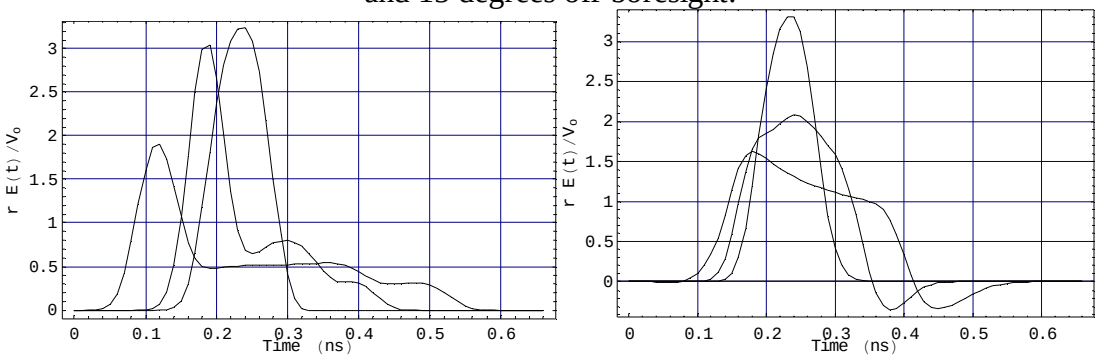

Figure 3.7. MIRA radiated field, f_f = 0.7, H-plane (left) and E-plane (right), at angles of 0, 7.5, and 15 degrees off-boresight.

IV. Experimental Validation

In order to demonstrate the MIRA experimentally, we built a model with a diameter of 46 cm (18 in), with adjustable feed arms. A diagram of the configuration as built is shown in Figures 4.1 and 4.2. It includes a solid 18-inch diameter parabolic reflector that slides along a set of four fixed feed arms. A servo motor controls the position of the reflector with respect to the feed, and a laptop computer communicates with the servo controller using a serial port.

The reflector was made of solid aluminum, and the feed arms were tin-coated copper. The F/D ratio was 0.5, and the feed impedance was 190 Ω. The antenna was fed with the so-called "splitter balun," of the type first described by C. Baum in [11]. This type of balun normally uses two 100 Ω cables connected in parallel at the feed end and in series at the antenna apex. However, it was difficult to find 0.141-inch diameter semi-rigid cable with 100 Ω impedance, so

we had to use 95 Ω cables. We believe the error is small enough for our purposes. Note also that the feed arms were designed to form a 190 Ω transmission line, which is consistent with the two 95 Ω lengths of feed cable.

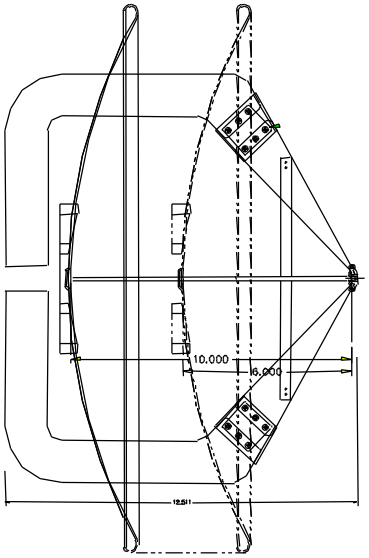

Figure 4.1. The MIRA, side view (left).

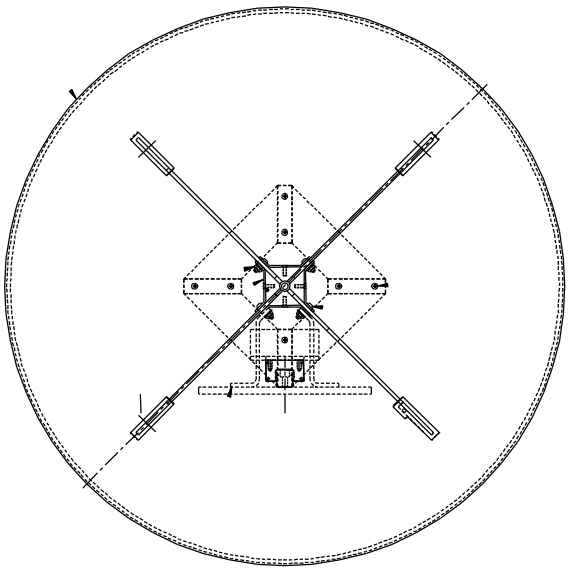

Figure 4.2. The MIRA, front view (right)

It was necessary to develop sensors that could be used to measure the radiated field. Standard derivative-type sensors have a very low sensitivity, so any measurements we made with our four-volt source would have been very noisy. Thus, we decided to develop a replicating sensor, which would replicate the incident electric field from the boresight direction. The design was essentially a half TEM horn mounted against a truncated ground plane (Figure 4.3). The ground plane was solid aluminum, and the conical plate was tin-plated copper. The impedance of the horn was 50 Ω, in order to avoid a mismatch to the 50 Ω electronics. The length of the horn was 45 cm. The top plate was supported with polystyrene foam for support.

The experimental test configuration for the antenna measurements is shown in Figure 4.4. In includes a Picosecond Pulse Labs 4015C step generator, which drives a TEM sensor. On the receive end, the Multifunction IRA receives the signal, which is then sampled by the SD24 sampling head and the Tektronix 11801B Digital Sampling Oscilloscope (DSO). Data is then downloaded to a computer for processing by way of a GPIB connection.

Before measuring the response of the MIRA, it is necessary to calibrate the TEM sensor. To do so, we measured the response of two identical TEM sensors, and then backed out the impulse response, using

$$V_{rec}(t) \;=\; \frac{1}{2\,p\,r\,c\,f_{g,tem}}\, h_{tem}(t) \circ h_{tem}(t) \circ \frac{dV_{src}(t)}{dt} \qquad (4.1)$$

where $h_{tem}(t)$ is the impulse response of the TEM sensor, $V_{src}(t)$ is the source voltage, and $V_{rec}(t)$ is the raw received voltage. Furthermore, $f_{g,tem}$ is the normalized impedance of the TEM sensor, c is the speed of light in free space, and the " ∘ " symbol indicates convolution. The only unknown in the above equation is $h_{tem}(t)$, and we solve for that using the techniques described in [12, Section III]. Note that we are using r to be the distance between the front edges of the two TEM sensors. There is some ambiguity here, since the sensors are large enough that there is some field variation over the length of the sensors.

First, we measured the source voltage, which is a clean step function with risetime of 28 ps. Next we took a measurement with the two identical TEM sensors, measured 3.35 meters apart. The resulting measured waveform consists of a relatively clean impulse, with t_{FWHM} =

50 ps. Next, the data is processed to extract $h_{tem}(t)$, and the result is shown in Figure 4.5 in the frequency domain, and Figure 4.6 in the time domain. The result in the time domain is an almost-clean impulse with t_{FWHM} = 33 ps.

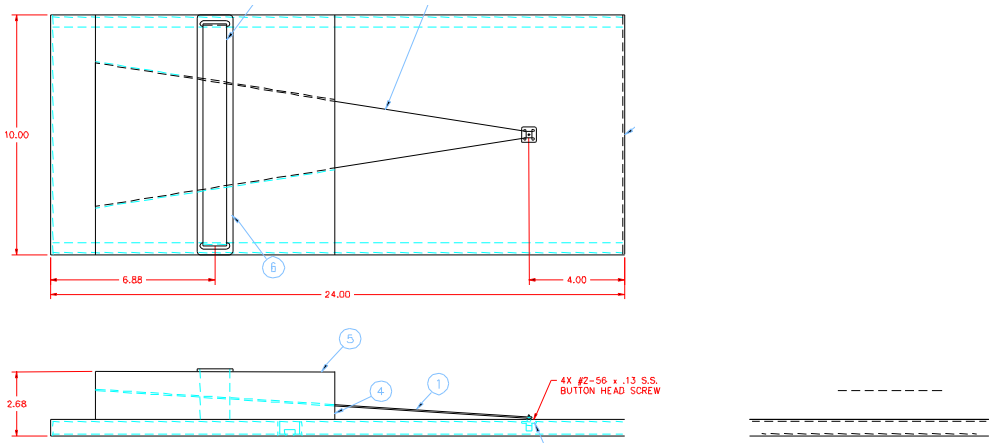

Figure 4.3. TEM Sensor. (Dimensions are inches.)

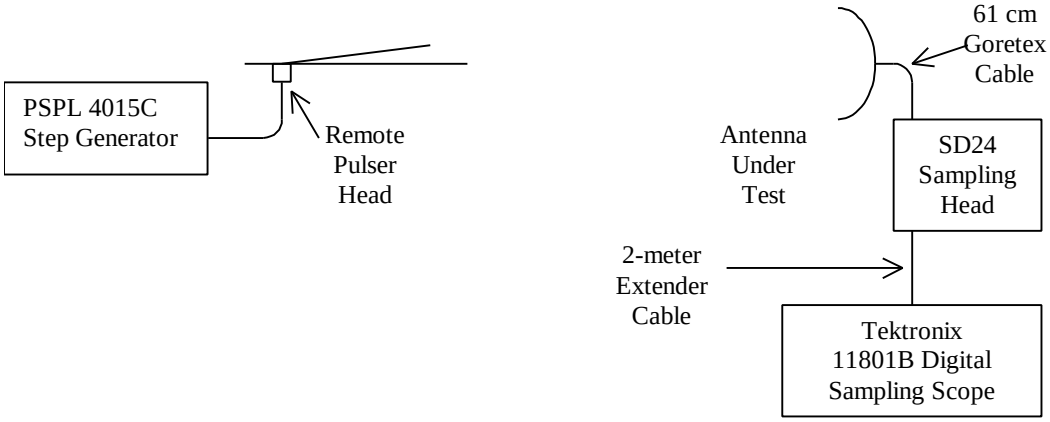

Figure 4.4.Experimental test setup

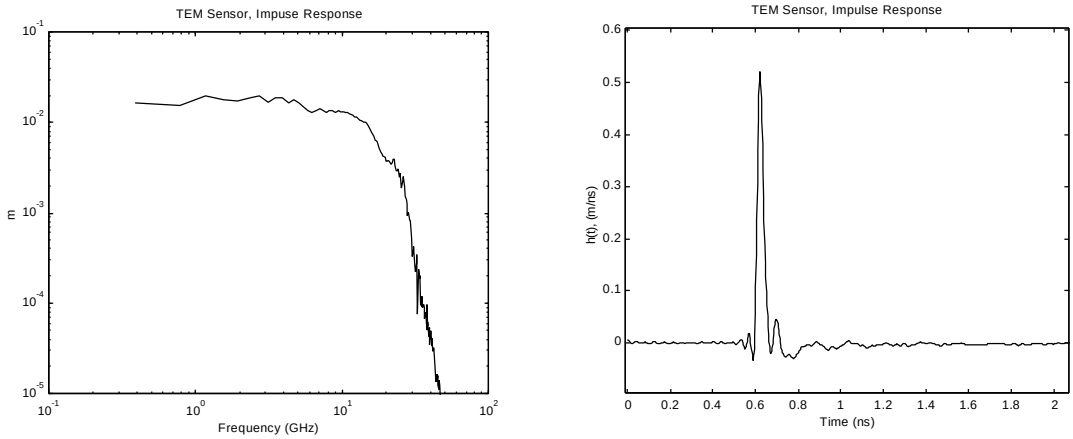

Figures 4.5 and 4.6. TEM sensor impulse response, $h_{tem}(w)$, in the frequency domain (left) and in the time domain (right).

Next, we provide the integral of $h_{tem}(t)$, shown in Figure 4.7. The degree to which this integral is a clean step function is a measure of whether we can use the TEM sensor data raw,

without correction. The integral is a step with some sag for the first 1.5 ns. (Note that some sag is expected, due to the characteristics of all TEM horns.) The jump in this integral gives us the effective height of the sensor. That is, assuming the voltage out of the sensor is (approximately) proportional to the incident field, the jump in this integral gives us the proportionality factor, or effective height, h_{eff}. We find that the magnitude of this jump is about 17 mm. Note that the plate is 31 mm above the ground plane in the aperture, so the measured h_{eff} is a little more than half of the physical aperture height. For an ideal geometry, we expect h_{eff} to be exactly half the physical aperture height [13]. Thus, our measurement of h_{eff} is consistent with theory.

Finally, we provide the TDR of the TEM sensor. The data is shown in Figure 4.10. A flat TDR indicates a good match to the 50 Ω input. We find the TDR is flat to within a few percent.

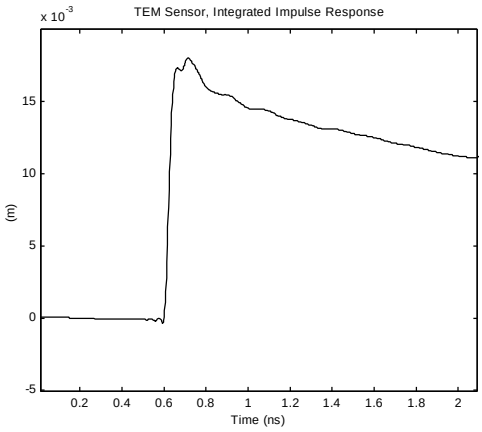

Figure 4.7. Integral of the TEM sensor impulse response.

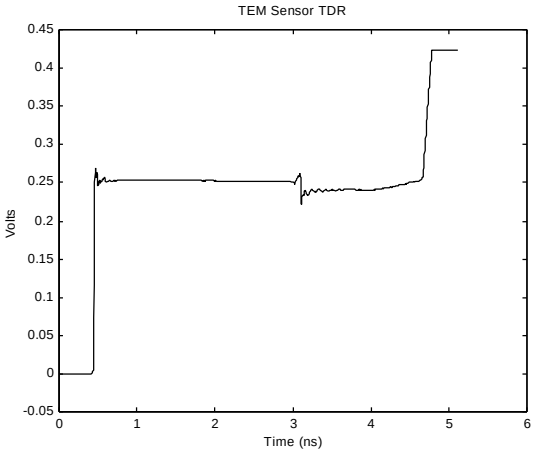

Figure 4.8. TDR of the TEM sensor (right).

Having characterized the sensor, we next measured the response of the MIRA. Note that we provide measurements of the MIRA that are slightly refined from those in [14], with various improvements to both the MIRA and the sensor. The sensor we used in the MIRA measurement presented here is slightly different that the sensor characterized above. The improvements to the sensor include a change in impedance to 100 Ω, and an improved support structure using teflon support posts instead of polystyrene foam. The new sensor, with its new impedance, has an improved sensitivity. Thus, for this sensor, h_a = 33 mm, and $h_{eff} = t \times h_a$, where t is the transmission coefficient from a 100 Ω TEM sensor to a 50 Ω cable (=0.667). So for the new sensor, h_{eff} = 0.667 × 33 mm = 22 mm, which is a 30% improvement over the previous value of 17 mm. Note that h_{eff} is roughly the proportionality factor between the incident field and the measured voltage in a 50 Ω cable. In addition, the FWHM of the one-way impulse response of 35 ps, which compares closely to 33 ps above. The length of the sensor is the same as the one characterized above.

The MIRA was also improved for this paper by reducing the size of the feed point, and by shifting the structural support away from the feed point. These improvements led to an improvement in the shape of the radiated field, as we will see.

The MIRA data was taken at a distance of 3.25 meters, using the 100 Ω TEM sensor to detect the signal. The boresight response for the MIRA is shown in Figure 4.9, in both the time and frequency domains. It displays the classic time-domain waveform of a low-level prepulse, followed by a sharp impulse, with Full Width Half Max of 80 ps. Note that this is raw received voltage. The impulse is clean, without any additional humps, so this is an improvement over the results of [14].

Next, we consider the antenna pattern as a function of angle off-boresight, and as a function of focus position. Using the definition of focal position provided earlier in equation (3.20), we made our measurements at focal positions of f_f = 1.0, 0.85, and 0.7. Furthermore, data were taken at positions of 0°, 7.5°, and 15° off boresight in the H-plane. The raw data for all nine waveforms is shown in Figure 4.10. Once again, we see the peak field is reduced as we go off-boresight, and as we become more defocused.

With the above data, we can estimate the beamwidths of this antenna for various focus settings in the H-plane. We use here the definition of Half Field Beam Width (HFBW) as described in Section III. These beam widths are tabulated in Table 4.1, and they are compared to the theoretical values calculated earlier in Section III. We find the trends agree, but the measured values are generally larger than the predictions.

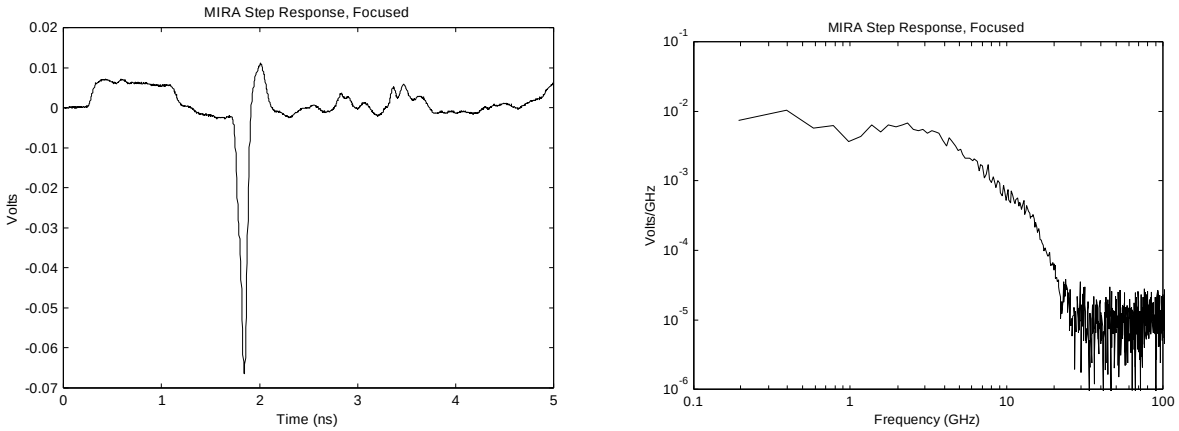

Figure 4.9. Boresight step response of the Multifunction IRA, in the time domain (left) and frequency domain (right).

Table 4.1. MIRA Half Field Beam Widths

	H-Plane Half Field Beam Width (HFBW)	
$f_f = F_2/F$	Theory (Section III)	Measurement
1.00	8°	12°
0.85	15°	28°
0.70	36°	60°

Next, we provide the TDR of the MIRA in Figure 4.12, using the 0.25-Volt source built into the SD-24 sampling head. We want to see a smooth match to 50 Ohms, but there are some reflections at the feed point. This represents some improvement over the TDR of the first version of the MIRA in [14], and we believe this is about the best we will be able to achieve.

Finally, we deconvolve the radiated field in focus from the sensor response and measurement system. The deconvolved h_{IRA}(t) is shown in Figure 4.12, in both the frequency and time domains. The FWHM of the resulting waveform is 53 ps. When we integrate the time domain function, we should obtain an area under the impulse of $a/2^{1/2}$, where a is the radius. After integrating the pulse, we find an area of 103 mm, compared to a theoretical value of 161 mm. Thus, we find a radiated impulse area of 64% of the expected value. We consider this to be reasonable agreement, although we would like to see better agreement in future designs.

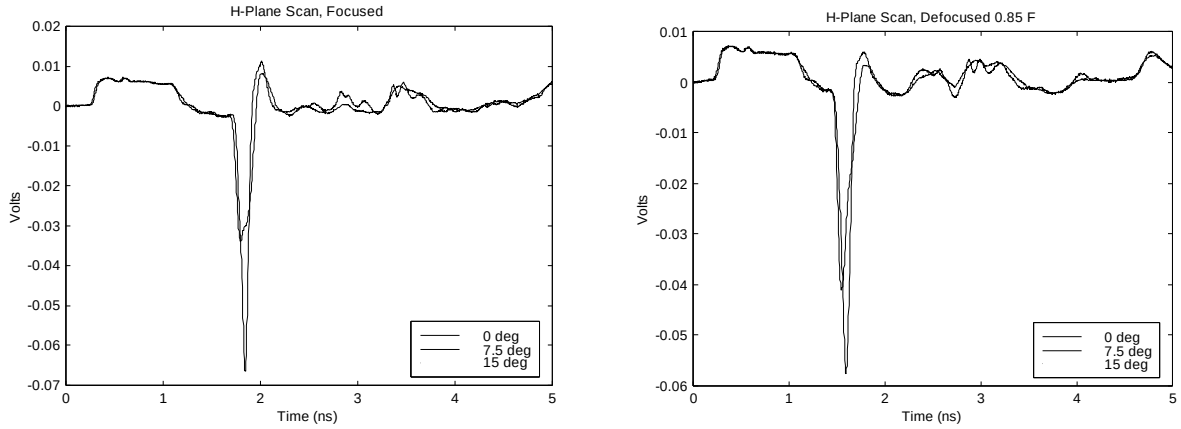

Figure 4.10. Antenna response for MIRA with f_f = 1.0 (left), and f_f = 0.85 (right). Antenna responses are for 0, 7.5, and 15 degrees off boresight in the H-plane.

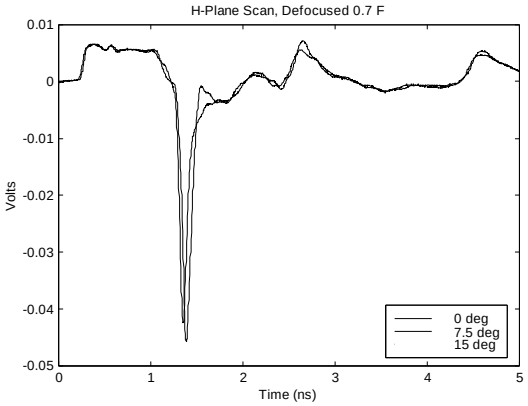

Figure 4.10 (cont'd) Same as above with f_f = 0.75.

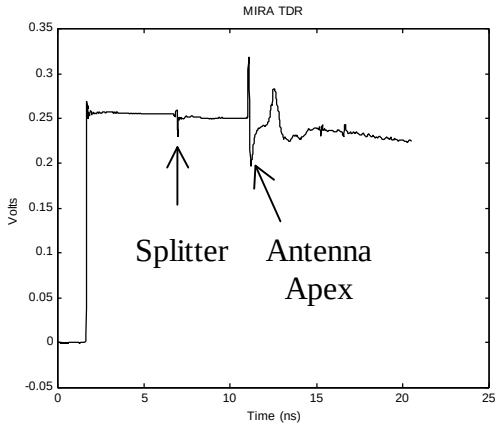

Figure 4.11. TDR of the MIRA.

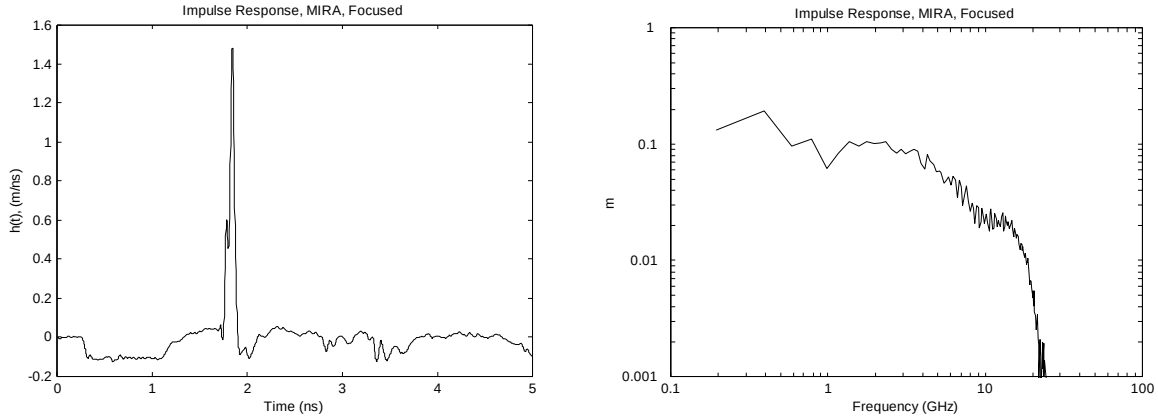

Figure 4.12. MIRA $h(t)$ after correction for the sensor, measurement system, and cabling, in the time domain (left) and frequency domain (right).

V. Conclusions

We have provided here the theory that describes the MIRA, and we have built and tested a model with 46 cm diameter. Satisfactory agreement was obtained between theory and measurements. The general technology of defocusing an IRA has been demonstrated, thereby increasing the flexibility of a single antenna to handle multiple missions.

References

1. C. E. Baum and E. G. Farr , Impulse Radiating Antennas, pp. 139-148 in H. L. Bertoni *et al* (eds.), *Ultra-Wideband, Short-Pulse Electromagnetics*, New York, Plenum Press, 1993.
2. E. G. Farr, C. E. Baum, and C. J. Buchenauer, Impulse Radiating Antennas, Part II, pp. 159-170 in L. Carin and L. B. Felsen (eds.), *Ultra-Wideband, Short-Pulse Electromagnetics 2*, New York, Plenum Press, 1995.
3. E. G. Farr, C. E. Baum, and C. J. Buchenauer, Impulse Radiating Antennas, Part III, pp. 43-56 in C. E. Baum *et al* (eds.), *Ultra-Wideband, Short-Pulse Electromagnetics 3*, New York, Plenum Press, 1997.
4. C. E. Baum, Radiation of Impulse-Like Transient Fields, Sensor and Simulation Note 321, November 25, 1989.
5. E. G. Farr and C. E. Baum, The Radiation Pattern of Reflector Impulse Radiating Antennas: Early-Time Response, Sensor and Simulation Note 358, June, 1993.
6. E. G. Farr, Off-Boresight Field of a Lens IRA, Sensor and Simulation Note 370, October 1994.
7. E. G. Farr and G. D. Sower, Design Principles of Half Impulse Radiating Antennas, Sensor and Simulation Note 390, December 1995.
8. E. G. Farr and C. A. Frost, Development of a Reflector IRA and a Solid Dielectric Lens IRA, Part I: Design, Predictions and Construction, Sensor and Simulation Note 396, April 1996.
9. C. J. Buchenauer and R. Marek, Antennas and Field Sensors for Time Domain Measurements: An Experimental Investigation, pp. 197-208 in L. Carin and L. B. Felsen (eds.) *Ultra-Wideband, Short-Pulse Electromagnetics 2*, New York, Plenum Press, 1995.
10. C. E. Baum, Focused Aperture Antennas, Sensor and Simulation Note 306, May 1987.
11, C. E. Baum, Configurations of TEM Feed for an IRA, Sensor and Simulation Note 327, April 1991.
12. E. G. Farr and C. A. Frost, Compact Ultra Short Pulse Fuzing Antenna Design and Measurements, Sensor and Simulation Note 380, June 1995.
13. C. E. Baum, Aperture Efficiencies for IRAs, Sensor and Simulation Note 328, June 1991.
14. E. G. Farr, C. E. Baum, and W. D. Prather, Multifunction Impulse Radiating Antennas: Theory and Experiment, Sensor and Simulation Note 413, November 1997.